

Integrated Covalent Organic Framework/Carbon Nanotube Composite as Li-Ion Positive Electrode with Ultra-High Rate Performance

Hui Gao, Qiang Zhu, Alex R. Neale, Mounib Bahri, Xue Wang, Haofan Yang, Lunjie Liu, Rob Clowes, Nigel D. Browning, Reiner Sebastian Sprick, Marc A. Little, Laurence J. Hardwick,* and Andrew I. Cooper*

Covalent organic frameworks (COFs) are promising electrode materials for Li-ion batteries. However, the utilization of redox-active sites embedded within COFs is often limited by the low intrinsic conductivities of bulk-grown material, resulting in poor electrochemical performance. Here, a general strategy is developed to improve the energy storage capability of COF-based electrodes by integrating COFs with carbon nanotubes (CNT). These COF composites feature an abundance of redox-active 2,7-diamino-9,10-phenanthrenequinone (DAPQ) based motifs, robust β -ketoenamine linkages, and well-defined mesopores. The composite materials (DAPQ-COFX—where X = wt% of CNT) are prepared by in situ polycondensation and have tube-type core-shell structures with intimately grown COF layers on the CNT surface. This synergistic structural design enables superior electrochemical performance: DAPQ-COF50 shows 95% utilization of redox-active sites, long cycling stability (76% retention after 3000 cycles at 2000 mA g⁻¹), and ultra-high rate capability, with 58% capacity retention at 50 A g⁻¹. This rate translates to charging times of ≈ 11 s (320 C), implying that DAPQ-COF50 holds excellent promise for high-power cells. Furthermore, the rate capability outperformed all previous reports for carbonyl-containing organic electrodes by an order of magnitude; indeed, this power density and the rapid (dis)charge time are competitive with electrochemical capacitors.

1. Introduction

Rechargeable Li-ion (Li-ion) batteries are widely used in daily life with ever-growing applications in the powering of portable devices, coupled with a marked shift towards electric vehicles. In addition to enlarging practical energy densities, new materials and technologies are needed to address the demand for higher power applications by enabling high current rates and rapid (dis)charge times without sacrificing cycling stability or lifetime. In this regard, electrochemical processes based on the simple, reversible redox reactions of organic electrode materials can often lead to higher rate performances when compared to inorganic electrode materials based on conventional intercalation reactions.^[1,2] Hence, organic electrode materials are promising candidates for the next generation of sustainable Li-ion batteries with a faster charging function.^[3,4] However, electrodes based on small organic molecules suffer from dissolution in organic electrolytes leading to poor cycling

H. Gao, Q. Zhu, X. Wang, H. Yang, L. Liu, R. Clowes, M. A. Little, A. I. Cooper
Materials Innovation Factory and Department of Chemistry
University of Liverpool
51 Oxford St, Liverpool L7 3NY, UK
E-mail: aicooper@liverpool.ac.uk

H. Gao, A. R. Neale, L. J. Hardwick
Stephenson Institute for Renewable Energy
Department of Chemistry
University of Liverpool
Peach St, Liverpool L69 7ZD, UK
E-mail: hardwick@liverpool.ac.uk

 The ORCID identification number(s) for the author(s) of this article can be found under <https://doi.org/10.1002/aenm.202101880>.

© 2021 The Authors. Advanced Energy Materials published by Wiley-VCH GmbH. This is an open access article under the terms of the Creative Commons Attribution License, which permits use, distribution and reproduction in any medium, provided the original work is properly cited.

DOI: 10.1002/aenm.202101880

M. Bahri, N. D. Browning
Albert Crewe Centre
University of Liverpool
Waterhouse Building, Block C, 1–3 Brownlow Street, Liverpool L69 3GL, UK
X. Wang, H. Yang
Leverhulme Research Centre for Functional Materials Design
University of Liverpool
Liverpool L69 7ZD, UK
R. S. Sprick
Department of Pure and Applied Chemistry
University of Strathclyde
Thomas Graham Building, 295 Cathedral Street, Glasgow G1 1XL, UK
A. I. Cooper
Leverhulme Research Centre for Functional Materials Design
University of Liverpool
51 Oxford St, Liverpool L7 3NY, UK

stabilities. Many efforts, including grafting the electroactive molecule onto a conductive backbone,^[5] forming a salt,^[6] or synthesizing insoluble polymeric materials,^[7,8] have been made to solving this dissolution problem. Polymeric materials are advantageous because, in addition to tunable insolubility, their molecular structures can be chemically tuned by employing different monomers to improve their performance.^[9,10]

COFs are a versatile class of crystalline porous solids formed by connecting organic precursors with covalent bonds to generate well-defined 2D or 3D frameworks.^[11–13] Advantages of COFs include their high structural modularity, which enables functional groups to be introduced into their frameworks in predictable positions, coupled with high porosity and uniform pore sizes.^[14] Unlike small organic molecules, COFs are typically insoluble in organic solvents and aqueous solutions. Also, synthetic strategies have been developed to generate COFs with excellent chemical stability.^[15,16] For example, a composite of a polyarylimide COF and CNT (2D-PAI@CNT COF) delivered 100% capacity retention after 8000 cycles, implying remarkable chemical stability of this COF composite material.^[17] In contrast to traditional polymers that typically lack long-range order, the ordered porosity in COFs can enable better diffusion of molecules to active sites.^[18] Therein, a 2D COF containing naphthalene diimide groups (TAPB-NDI COF) with a Brunauer–Emmett–Teller surface area (S_{BET}) of $490 \text{ m}^2 \text{ g}^{-1}$ was shown to deliver 95% of its theoretical capacity (63 mAh g^{-1}) under $C/20$. By contrast, an amorphous polymer analog with a S_{BET} of $20 \text{ m}^2 \text{ g}^{-1}$ only delivered 25% of its theoretical capacity under the same conditions.^[19] Moreover, interlayer π - π stacking interactions between COFs layers have been shown to improve conductivity.^[20] Recently, several studies have used COFs as the active material in the electrodes of Li-ion batteries.^[17,21–24] However, since COFs often exhibit poor intrinsic conductivities, conductive coatings or additives are often added to improve their electron transfer and rate performance in batteries.^[15,25–28] In this regard, a redox-active

polyimide COF ($D_{\text{TP}}\text{-A}_{\text{NDI}}\text{-COF}$) was reported as a positive electrode for Li-ion batteries where only 5% of the redox-active sites were utilized at 12 C.^[15] By contrast, a composite of the same polyimide COF and CNT ($D_{\text{TP}}\text{-A}_{\text{NDI}}\text{-COF@CNTs}$) exhibited 71% utilization of redox-active sites under the same conditions.^[15] A 2D microporous COF and CNT composite electrode, 2D CCP-HATN@CNT, synthesized by in situ polymerization on CNT, exhibited a high capacity of 116 mAh g^{-1} with 99% utilization of its redox-active sites, and good cycling stability (91% after 1000 cycles) and rate capability (82%, 1.0 A g^{-1} versus 0.1 A g^{-1}).^[18] In addition, bulk-grown COF-based electrodes have been shown to exhibit sluggish diffusion kinetics, which has limited their performance in batteries. However, exfoliation of the COF layers has been shown to improve performance.^[29–31] For example, a redox-active anthraquinone containing exfoliated COF layers with shorter Li-ion diffusion pathways exhibited higher capacity than the bulk-grown COF at the same current density.^[29]

Here, we investigated the electrochemical properties of the 2,7-diamino-9,10-phenanthrenequinone (DAPQ) motif in organic batteries. DAPQ contains two redox-active carbonyl groups that can undergo reversible reactions with Li^+ ions. By itself, DAPQ was found to deliver a high initial capacity of 204 mAh g^{-1} at 500 mA g^{-1} in Li-ion half-cells, but its capacity rapidly decreased to 21 mAh g^{-1} after 10 cycles as DAPQ dissolved into the electrolyte, and similar behavior being reported for structurally related organic molecules.^[32] To improve the electrochemical performance and cycling stability of the DAPQ motif in organic batteries, we instead designed a composite of a mesoporous 2D COF (DAPQ-COF, **Figure 1**) thinly coated around multi-wall carbon nanotubes (CNT). An advantage of the phenanthrenequinone units in DAPQ-COF is that they have a high discharge potential of 2.6 V vs. Li^+/Li because of a three-fold charge stabilization mechanism,^[33] and its π conjugation can stabilize charge and interlayer packing in its extended crystal structure. DAPQ-COF was found to have a

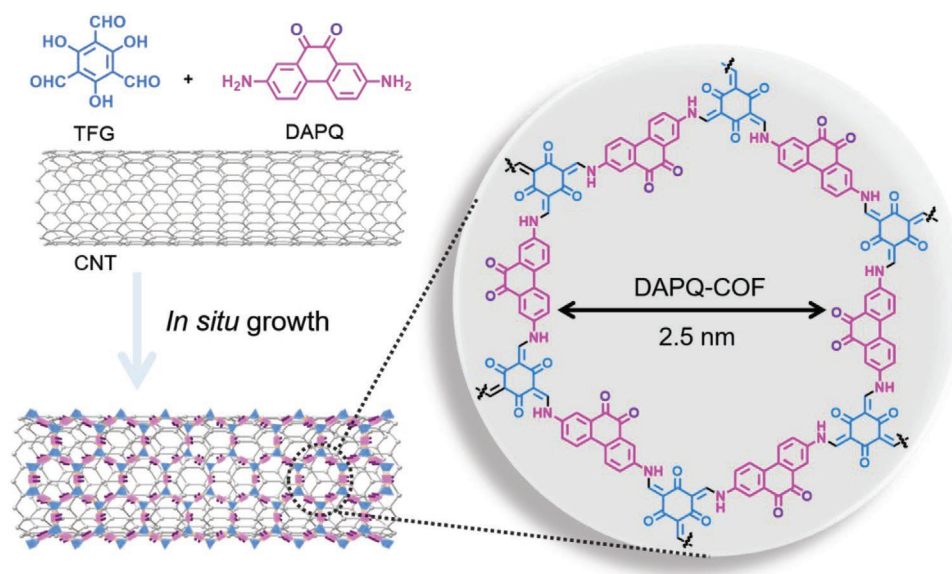


Figure 1. Scheme for the synthesis of DAPQ-COF and CNT composite via in situ growth.

low specific capacity of 73 mAh g⁻¹ at 500 mA g⁻¹ in a Li-ion cell. However, the electrochemical performance was greatly enhanced by forming the tube-type core-shell structure of the composites (DAPQ-COFX). Using this approach, we achieved specific capacities of up to 162 mAh g⁻¹ at 500 mA g⁻¹. By varying the composition of the DAPQ-COFX composite, it was found that DAPQ-COF50, which contained 50 wt% of CNT, exhibited the highest utilization of the redox-active sites (95%). Notably, the DAPQ-COF50 composite presents the best rate performance in COF-based electrode materials reported so far, facilitating ultrafast charge/discharge rates as high as 50 A g⁻¹—this means that the device can be fully charged in just 11 s.

2. Results and Discussion

2.1. Preparation and Characterization of DAPQ-COFs

DAPQ-COF was synthesized via a Schiff-base condensation reaction of 1,3,5-triformylphloroglucinol (TFG) with DAPQ to afford the crystalline 2D COF in a yield of 91% (Figure 1, see Experimental section for reaction conditions). The condensation reaction is followed by an irreversible keto-enol tautomerization, which enhances the chemical stability and reduces the solubility of the COF.^[34] After optimizing the synthetic conditions by varying the reaction solvent and temperature, it was found that a mesitylene/1,4-dioxane solvent mixture and reaction temperature of 120 °C formed the COF product with the highest crystallinity (Table S1, Supporting Information, Line 16). Composites of DAPQ-COF and CNT were synthesized using the same procedure by adding 10, 30, and 50 wt% of CNT into the reaction mixtures to produce the DAPQ-COFX composites, where X = 10, 30, and 50 wt% of CNT. For this study, catalyst-free, multi-walled CNTs were used with outer diameter and length ranges of 7–15 nm and 0.5–10 μm, respectively. For brevity, these materials are simply abbreviated to CNT throughout. All available properties for the CNT are provided in the Experimental section, and further characterizations, including Raman spectroscopy and electron micrographs, are provided in the Supporting Information (Figure S1 and Table S2, Supporting Information).

DAPQ-COF and DAPQ-COFX composites were characterized by Fourier-transform infrared spectroscopy (FT-IR) (Figure S2, Supporting Information). The absence of N–H stretching bands at 3436, 3340, and 3220 cm⁻¹ from the DAPQ precursor in DAPQ-COF or any of the DAPQ-COFX composites indicated complete consumption of DAPQ in the polycondensation reactions. Bands at 1250 and 1572 cm⁻¹ in the spectra of DAPQ-COF and the DAPQ-COFX composites were assigned to β-ketoenamine C–N moieties and to ν_{C=C}, respectively, indicating the COF was in the β-ketoenamine form^[34] as shown in Figure 1. ¹³C cross-polarization magic angle spinning (CP-MAS) solid-state NMR spectroscopy was also used to characterize DAPQ-COF (Figure 2a). Peaks at 146 and 108 ppm were assigned to the enamine carbon (=CNH) and α-enamine carbon, respectively, confirming the formation of the β-ketoenamine-linked COF.^[35] Furthermore, the aldehyde carbon signal of TFG at 192 ppm (Figure S3, Supporting

Information) was not found in the CP-MAS spectrum of DAPQ-COF.

Powder X-ray diffraction (PXRD) was used to confirm the structure of DAPQ-COF and to assess its crystallinity in the DAPQ-COFX composites. The experimental PXRD pattern of DAPQ-COF matched the simulated PXRD pattern of the aligned A-A stacked model closely (Figure 2b and Figure S4, Supporting Information). A Pawley refinement confirmed that the PXRD data was consistent with DAPQ-COF having the same hexagonal *P6/m* symmetry (*a* = *b* = 29.42 Å, *c* = 3.62 Å, *V* = 2717.5 Å³) and comparable dimensions as the A-A stacked model (Figure 2b). The PXRD patterns of the DAPQ-COFX composites showed that the addition of CNT decreased the crystallinity of the DAPQ-COF, with DAPQ-COF50 estimated to be the least crystalline as assessed by PXRD (Figure S5, Supporting Information). However, the PXRD patterns indicated that DAPQ-COF still adopted the same structure in the DAPQ-COFX composites. High-resolution transmission electron microscopy (HR-TEM) images (Figure 2d,e,g,h) revealed that DAPQ-COF has an ordered structure with hexagonal pores oriented along its crystallographic *c* axis (area outlined in yellow, Figure 2h). Both HR-TEM images and the corresponding fast Fourier transformation (FFT) of the DAPQ-COF confirmed its crystallinity (Figure 2e). Tube-type core-shell structures of DAPQ-COFX with the COF structure grown around the external surface of the CNT were observed (Figure 2c,f,i). The COF layers grown on the CNTs surface retain their crystallinity, and thicker COF layers were observed for DAPQ-COF10 than DAPQ-COF30 and DAPQ-COF50. The TEM image of the pure CNTs used in this work is also provided in Figure S6 for reference. The morphologies of DAPQ-COF and the DAPQ-COFX composites were recorded by scanning electron microscope (SEM, Figure S7, Supporting Information). DAPQ-COF was found to have a rod-like morphology in the SEM images. The morphology difference of DAPQ-COF10, DAPQ-COF30, and DAPQ-COF50 is that the latter appears to retain bulk CNT morphology, supporting a uniform ≈10 nm COF layer on the surface. For DAPQ-COF10, we only observed rod-shaped particles, implying the CNTs were covered entirely in a thicker layer of COF.

PXRD patterns (Figure S8, Supporting Information) and FT-IR spectra (Figure S9, Supporting Information) of DAPQ-COF collected before and after 24 h exposure to *N,N*-dimethylformamide, *N*-methyl-2-pyrrolidone, water, 1 M and 12 M HCl (aq.) were comparable, indicating DAPQ-COF maintained its structure after being submerged in these liquids. Nitrogen sorption isotherms for DAPQ-COF showed that it had a type-II isotherm with a *S*_{BET} of 245 m² g⁻¹ and an uptake of 5.8 mmol g⁻¹ at 1 bar (Figure S10, Supporting Information), with no changes to the COF structure observed after this measurement (Figure S11, Supporting Information). The pore size of 2.2 nm agrees with the pore size in the A-A stacked model (2.5 nm) (Figure 1). DAPQ-COF10, DAPQ-COF30, and DAPQ-COF50 also had type-II isotherms and uptakes of 11.7, 18.9, and 22.5 mmol g⁻¹ at 77.3 K and 1 bar, respectively (Table S3 and Figure S10, Supporting Information). The DAPQ-COFX composites exhibited reduced surface areas (DAPQ-COF10 < DAPQ-COF30 < DAPQ-COF50) relative to both pure COF and CNT components.

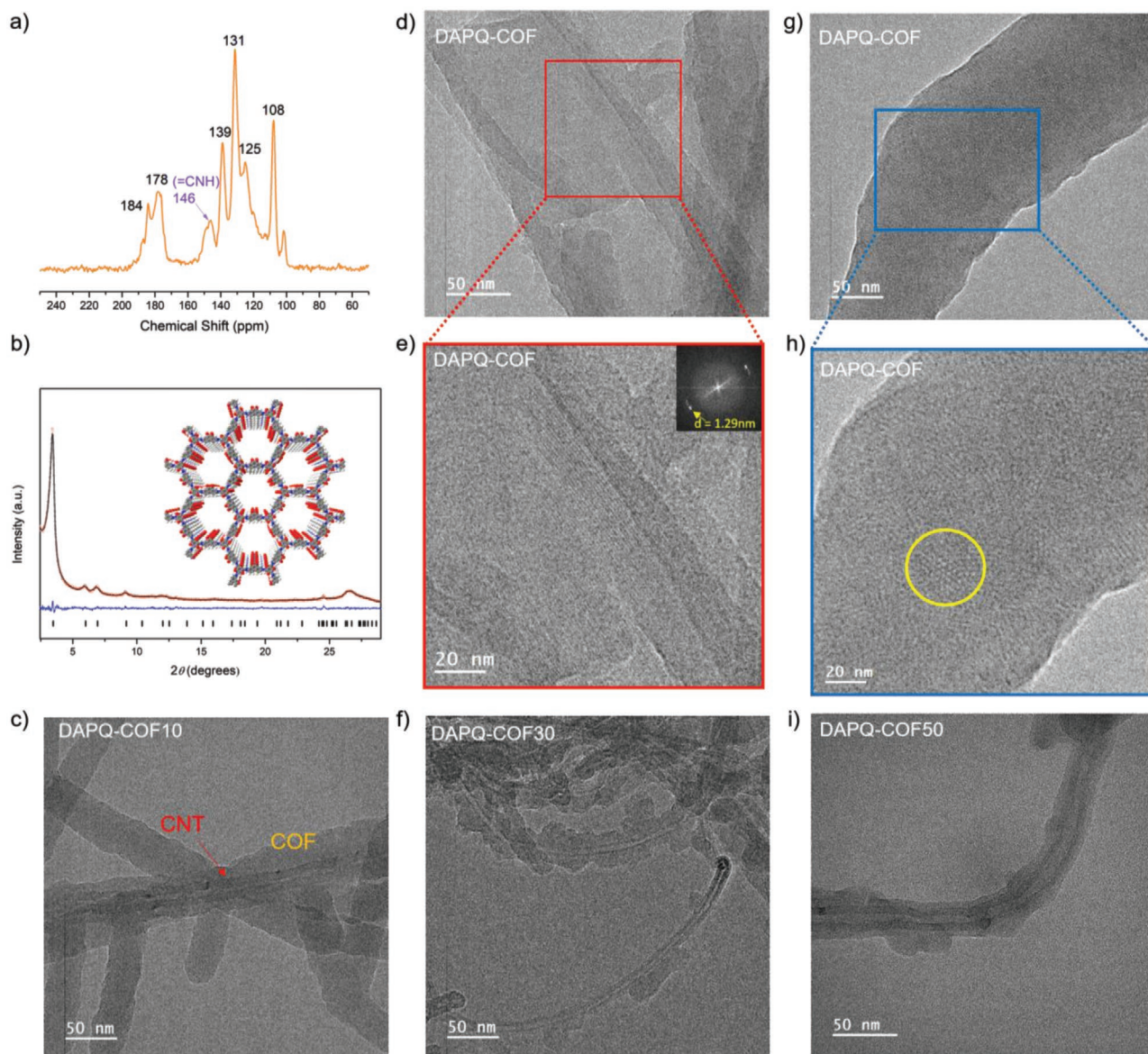


Figure 2. a) $^{13}\text{C}\{^1\text{H}\}$ solid-state NMR CP-MAS spectrum of DAPQ-COF; b) Crystal structure of DAPQ-COF showing its eclipsed A-A stacking model along the crystallographic c axis (inset). PXRD pattern fitting of DAPQ-COF with Pawley refinement ($\text{Cu-K}\alpha$). Red circles: experimental PXRD pattern, black line: fitting pattern, blue curve: difference between experimental and refinement, black bars: reflection positions, ($P6/m$, $a = b = 29.42 \text{ \AA}$, $c = 3.62 \text{ \AA}$, $V = 2717.5 \text{ \AA}^3$, $R_p = 2.21\%$, $R_{wp} = 3.17\%$); d,e,g,h) HR-TEM images of DAPQ-COF (inset shows FFT image showing the crystalline structure with a d -spacing of 1.29 nm); TEM image of c) DAPQ-COF10, f) DAPQ-COF30, and i) DAPQ-COF50 showing tube-type core-shell structure of composites. Scale bars are included.

2.2. Electrochemical Characterization

Next, the electrochemical performance of DAPQ-COF and the DAPQ-COFX composites as positive electrodes for Li-ion coin cells was investigated (Figure 3). Coin cells were assembled with DAPQ-COF or the DAPQ-COFX composites as the positive electrode and Li as the counter electrode. Li bis(trifluoromethanesulfonyl)imide (LiTFSI) (1 M in 1,3-dioxolane/1,2-dimethoxyethane (1:1 v/v)) was used as the electrolyte formulation because it supports good performance in organic cathode materials.^[8,22,36] By contrast, Li-ion battery electrolytes based on Li hexafluorophosphate salt in organic

carbonates showed poor cycling performance for the DAPQ-COF-based materials investigated here (Figure S12, Supporting Information).

Cyclic voltammetry (CV) of DAPQ-COF and the DAPQ-COFX composites was performed on the coin cells at 0.1 mV s^{-1} in a potential window of $1.5\text{--}3.2 \text{ V}$ (Figure 3a). DAPQ-COF and the DAPQ-COFX composites had similarly shaped CV curves with two pairs of redox peaks centered around 2.8 and 2.3 V , which corresponds to the two-step two-electron reaction of the pair of carbonyl groups in each DAPQ based motif of the COF.^[33] Furthermore, the peak current densities and integral charge (based on the mass of DAPQ-COF as the active material)

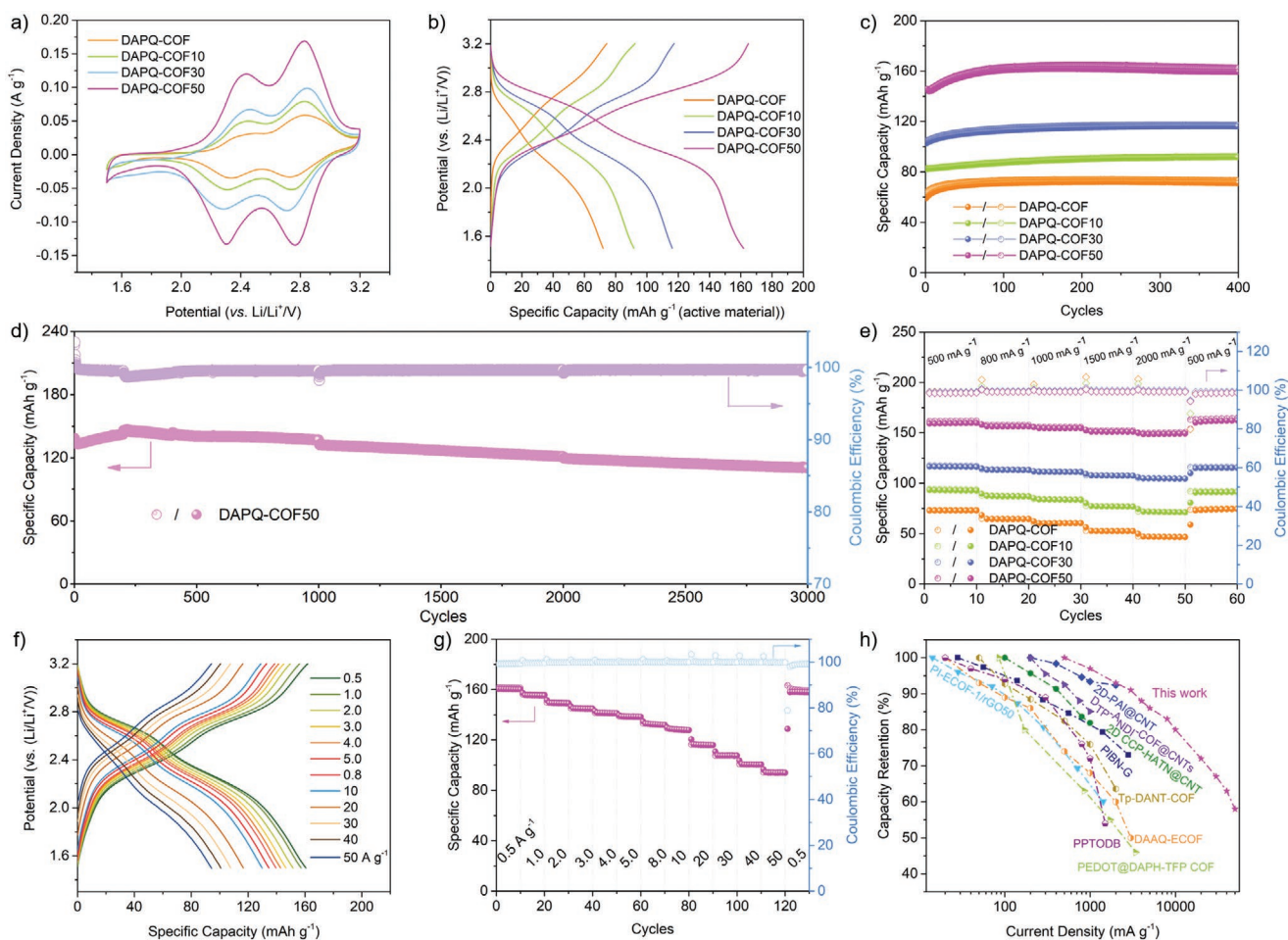


Figure 3. a) CV profiles at a scan rate of 0.1 mV s^{-1} ; b) Charge/discharge profiles at 500 mA g^{-1} ; c) Cycling performances over 400 cycles at 500 mA g^{-1} for DAPQ-COF, DAPQ-COF10, DAPQ-COF30, and DAPQ-COF50; d) Long-term cycling stability of DAPQ-COF50 at 2000 mA g^{-1} ; e) Rate performance of DAPQ-COF, DAPQ-COF10, DAPQ-COF30, and DAPQ-COF50; f) Charge/discharge profile of DAPQ-COF50 at different current density; g) High rate performance of DAPQ-COF50; h) Comparison of the rate performance to other COFs cathodes (reference information and abbreviations for comparative data shown in the Supporting Information). For Figures c,d,e,g, charge and discharge capacities are represented by open and solid symbols, respectively.

increased as the mass ratio of CNT in the DAPQ-COFX composite was increased. DAPQ-COF50 has the highest integral charge area, indicating more effective utilization of redox-active sites in DAPQ-COF50 than DAPQ-COF, which may be because the intrinsically conductive CNTs in the composites enhances charge transport throughout the bulk electrode. It is, however, important to note that all electrode composites (DAPQ-COF and the DAPQ-COFX composites) also contained conductive carbon black (30% by weight for DAPQ-COF and 20% by weight for the DAPQ-COFX composites).

Galvanostatic charge/discharge tests were carried out over a voltage window of 1.5 to 3.2 V for all the positive electrodes (Figure 3b). The sloping plateaus in the voltage profiles agree well with the corresponding CV curves, likewise being attributed to the reversible reduction/oxidation of the carbonyl groups in the DAPQ units. The average discharge potential of DAPQ-COFs and DAPQ-COFX composite is about 2.56 V, which is higher than most of the reported COF-based positive electrodes (Table S4, Supporting Information).^[37–39] DAPQ-COF contains an abundance of electron-withdrawing groups

(C=O), which could decrease the lowest unoccupied molecular orbital level and, in turn, raise the reduction potential.^[40] At the current density of 500 mA g^{-1} , DAPQ-COF has a specific capacity of 73 mAh g^{-1} , corresponding to only 46% of its theoretical capacity (based on its theoretical specific capacity of 157 mAh g^{-1} , see Figure S13, Supporting Information, for full details). However, in DAPQ-COF10, DAPQ-COF30, and DAPQ-COF50 the specific capacity at 500 mA g^{-1} improved to 92, 116, and 162 mAh g^{-1} , respectively, based on the mass of the DAPQ-COF active material. For comparison, the charge/discharge profiles based on the total mass of the DAPQ-COF, CNT, and carbon black in the electrode are shown in Figure S14, Supporting Information. Taking into account that CNT can contribute 1, 6, and 13 mAh g^{-1} to the specific capacities of DAPQ-COF10, DAPQ-COF30, and DAPQ-COF50 (see Table S5 and Figure S15–S20, Supporting Information, for full details), the utilization of redox-active sites increased to 58, 70, and 95% in DAPQ-COF10, DAPQ-COF30, and DAPQ-COF50, respectively. Moreover, DAPQ-COF and DAPQ-COFX retained a near-constant capacity after 400 cycles highlighting their excellent

electrochemical stability (Figure 3c). As shown in Table S4, Supporting Information, the capacity and cycling performance of DAPQ-COF50 outperforms a range of other COF-based positive electrodes. For example, a composite of rGO and polyimide-based COF (PI-ECOF-1/rGO50) delivered an initial capacity of 167 mAh g⁻¹ under a current density of 14.2 mA g⁻¹ but lost 30% of its capacity after 300 cycles at 142 mA g⁻¹.^[22] An exfoliated COF with anthraquinone redox-active units (DAAQ-ECOF) delivered a lower initial capacity of 145 mAh g⁻¹ at 20 mA g⁻¹ but exhibited good capacity retention after 1800 cycles (92%) at 500 mA g⁻¹.^[29] A 2D poly(imide-benzoquinone) COF (PIBN-G) electrode delivered the highest initial capacity (271 mAh g⁻¹ at 0.1 C) for COF-based positive electrode, but its capacity decreased by 12% over 300 cycles at 5 C.^[39]

When the DAPQ monomer was used as the positive electrode, it delivered an initial capacity of 204 mAh g⁻¹ at 500 mA g⁻¹ (91% of its theoretical specific capacity) (Figure S21, Supporting Information), which is higher than DAPQ-COF and the DAPQ-COFX composites, but its capacity rapidly decreased to 21 mAh g⁻¹ after only 10 cycles. We attribute the rapid reduction in performance of the DAPQ monomer to its dissolving in the electrolyte, which then caused it to turn blue (Figure S22, Supporting Information). Conversely, DAPQ-COF and the DAPQ-COFX composites had low solubility in the electrolyte, and only a trace amount of the DAPQ monomer was identified in the UV-Vis spectra of the electrode-soaked solvents (Figure S23, Supporting Information). The negligible solubility of DAPQ-COF and the DAPQ-COFX composites in the electrolyte significantly improved their cycling performance. An amorphous polymer sample was also prepared by reacting the DAPQ and TFG monomers in dimethylacetamide and mesitylene solvent for comparison (Figure S24, Supporting Information). By contrast to DAPQ-COF by itself, the amorphous DAPQ and TFG containing sample had a much lower S_{BET} of 52 m² g⁻¹ (Figure S25, Supporting Information) and delivered a much lower capacity of 19 mAh g⁻¹ at 500 mA g⁻¹ (Figures S26 and S27, Supporting Information). Here, 19 mAh g⁻¹ corresponds to 12% utilization of the redox-active sites and highlights that the lower porosity hinders electrolyte diffusion.^[41]

Long-term cycling stability is an important criterion to estimate cell performance. Here, the long-term cycling properties of the optimized composite, DAPQ-COF50, were studied by repeated charge/discharge cycling experiments at a current density of 2000 mA g⁻¹ (about 12.7 C) (Figure 3d). DAPQ-COF50 reached a maximum capacity of 146 mAh g⁻¹ over the first ≈200 cycles, while the Coulombic efficiency was nearly constant at ≈99.97% over 3000 charge/discharge cycles. DAPQ-COF50 had a 76% retention of the highest recorded capacity (a capacity loss of ≈0.008% per cycle), indicating stable active site utilization and good cycling stability. The cycling performance of DAPQ-COF50 outperforms many other COFs reported in the literature (see Table S4, Supporting Information, for abbreviations, performance, and citation information). For example, Tb-DANT-COF exhibited a 75% capacity retention after 300 charge/discharge cycles at 500 mA g⁻¹,^[42] PPTODB delivered 88% of the initial capacity after 150 charge-discharge cycles under 20 mA g⁻¹,^[43] and 2D-PAI@CNT has the highest cycling performance reported (100% capacity retention after 8000 charge-discharge

cycles at 500 mA g⁻¹).^[17] No change to the IR spectra or the morphology (as measured by SEM) of the DAPQ-COF50 electrode was observed after 400 times charge/discharge cycles (Figures S28 and S29, Supporting Information), indicating good electrode stability.

The rate capabilities of DAPQ-COF and the DAPQ-COFX composites were then investigated over the range 500–2000 mA g⁻¹ (Figure 3e). The capacity retention at 2000 mA g⁻¹ for DAPQ-COF, DAPQ-COF10, DAPQ-COF30, and DAPQ-COF50 were 64%, 77%, 90%, and 92%. The relatively thinner and intimately contacting layers in DAPQ-COF50 (and to some extent DAPQ-COF30) improves overall electrochemical accessibility that is unhindered even at high rates of (dis)charge. In addition, the capacity of all composites recovered to the initial values once the current was reduced back to 500 mA g⁻¹ and Coulombic efficiency remained at approximately 100% for all cycles, indicating the higher rates of charge/discharge did not impact upon material stability in this measurement range.

We next looked more in-depth at our best performing COF-composite, DAPQ-COF50, to demonstrate how the preparation of this material allows the boundaries of rate performance to be expanded. The rate performance of DAPQ-COF50 was tested up to 50000 mA g⁻¹. Despite some reasonable overpotential increases at the highest currents, the voltage profiles consistently feature the same sloped plateaus associated with Faradaic discharge and charge reactions, implying the excellent transport properties of both Li⁺ ions and electrons at/within the DAPQ-COF50 electrodes (Figure 3f). The rate performance for DAPQ-COF50 from 500 to 50000 mA g⁻¹ shows excellent capacity retention and no loss of Coulombic efficiency at ultra-high current densities (Figure 3g). DAPQ-COF50 delivers 129 mAh g⁻¹ at 10000 mA g⁻¹, equating to a retention of 80% of the capacity attained at 500 mA g⁻¹. DAPQ-COF50 still provides excellent rate performance and delivers 94 mAh g⁻¹ discharge capacities (58% retention) when the current density is pushed further to ultra-fast discharge/charge rates at 50000 mA g⁻¹. For context, this upper testing limit of current density equates to an approximate C-rate of 320 C, corresponding to a full charge or discharge in ≈11 s. The C-rate is defined as the current required to completely (dis)charge the electrode in 1 h, based on the theoretical capacity of the active material. Remarkably, the ultra-high current cycling steps did not appear to affect the material stability since the capacity at 500 mA g⁻¹ recovered to the initial values.

The rate capability of DAPQ-COF50 is superior to those of the recently reported COF cathodes; indeed, the upper current density limit achieved here exceeds earlier works by an order of magnitude (Figure 3h and Table S6, Supporting Information). For example, a poly(imide-benzoquinone) COF on graphene (PIBN-G) showed 73% of the capacity at 10 C, compared with the capacity at 1 C.^[40] A COF containing redox-active naphthalene diimide walls on CNT (D_{TP-A_{NDI}}-COF@CNTs) retained 85% capacity under 1000 mA g⁻¹ (12 C) versus the capacity at 200 mA g⁻¹ (2.4 C).^[15] A polyarylimide hybrid (2D-PAI@CNT) has 92% of the capacity when discharged at 19.2 C.^[17] However, there have yet been no tests beyond 5000 mA g⁻¹ in COF cathodes materials reported so far. Comparable current densities have previously been reported for a non-COF organic electrode material, wherein a linear polymer (PNDI-T2) was reportedly

measured up to 500 C, corresponding to the absolute current density of $27\,100\text{ mA g}^{-1}$, but for comparison, this material only exhibited a capacity of 23 mAh g^{-1} .^[44] In our case, we tested the DAPQ-COF50 based cathode up to $50\,000\text{ mA g}^{-1}$ and it delivered a capacity of 94 mAh g^{-1} , corresponding to a high power density of $\approx 110\text{ kW kg}^{-1}$. This magnitude of power density, and the rapid charge/discharge times, would be competitive with electrochemical capacitors.^[45] For further comparison of the rate performance of our material with prior literature, we plot the comparison data as functions of absolute capacities and in terms of C-rates in the Supporting Information (Figures S30–S33, Supporting Information). Figure S30, Supporting Information, shows that while a 2D poly(imide-benzoquinone) COF, PIBN-G, has the highest specific capacity over a C-rate range from 0.1 to 10 C,^[17] the absolute specific capacity delivered by DAPQ-COF50 under different C-rate surpasses many other reported COF electrodes, where the C-rates are based on the theoretical capacity of each individual material. The same trend can be seen in Figure S31, Supporting Information, where the absolute specific capacity of the COFs electrode as a function of gravimetric current densities is compared. When compared in this way with these other materials, the capacity retention as a function of the C-rate (Figure S32, Supporting Information), DAPQ-COF50 shows the best capacity retention, with 58% capacity retention at 320 C versus 3.2 C. Furthermore, Figure S33, Supporting Information, shows the analogous non-logarithmic scaling of Figure 3h to highlight the dramatic scale of capacity retention achieved at the ultra-high current densities used here (i.e., $50\,000\text{ mA g}^{-1}$ or 320 C). For example, the capacity retention of a pyrene-4,5,9,10-tetraone based COF (PPTODB) electrode dropped to less than 55% at

1500 mA g^{-1} ,^[43] and a phenazine-based 2D COF (PEDOT@ DAPH-TFP COF) had 55% capacity retention at 1710 mA g^{-1} .^[37] Figure S33b, Supporting Information, shows an enlarged section of the current density plot below 3750 mA g^{-1} to give a clearer comparison of the improved capacity retention of DAPQ-COF50 relative to other reported COF electrodes.

2.3. Importance of the Tube-type Core-shell Composite Structure

We next explored whether the intricate tube-type core-shell structure of the DAPQ-COFX composites was required to obtain the high rate performances. A sample of DAPQ-COF and CNT was prepared by ball milling dry samples of DAPQ-COF and CNT in a 1:1 mass ratio (DAPQ-COF/CNT). When the physical mixture DAPQ-COF/CNT was used as the active material, the resulting coin cell had a capacity of 129 mAh g^{-1} at 500 mA g^{-1} (Figure 4), which is 32 mAh g^{-1} lower than DAPQ-COF50 under the same conditions (translating to a 20% lower gravimetric capacity). Hence, the in situ grown DAPQ-COF50 composite, with its tube-type core-shell structure with DAPQ-COF grown as a thin crystalline outer layer on the CNTs, enabled better electrochemical accessibility of active sites. The rate performance of DAPQ-COF50 was also better than DAPQ-COF/CNT. For example, DAPQ-COF50 retained 58% of its capacity at 50 A g^{-1} , while DAPQ-COF/CNT only retained 34% of its capacity under the same conditions (Figure 4c). In absolute terms, this equates to the DAPQ-COF50 (94 mAh g^{-1}) delivering more than twice the capacity of the DAPQ-COF/CNT (44 mAh g^{-1}), highlighting the importance of the core-shell composite structure. Furthermore, a small reduction in the

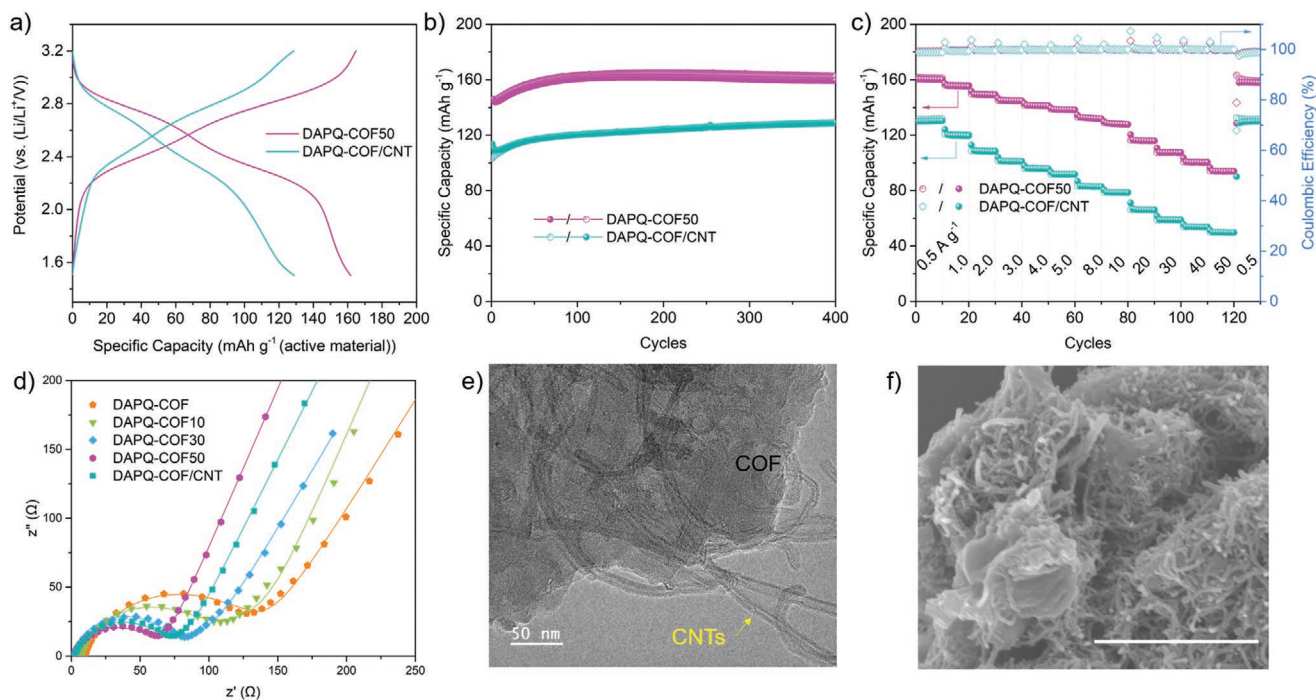


Figure 4. a) Charge/discharge profiles at 500 mA g^{-1} ; b) Cycling performances over 400 cycles at 500 mA g^{-1} ; c) High rate performance of DAPQ-COF50, and DAPQ-COF/CNT; d) Nyquist plots at open-circuit potential for DAPQ-COF, DAPQ-COF10, DAPQ-COF30, DAPQ-COF50, and DAPQ-COF/CNT (solid lines represent the simulated EIS data); e) TEM image of DAPQ-COF/CNT; f) SEM image of DAPQ-COF/CNT (scale bar: $1\text{ }\mu\text{m}$).

charge transfer resistance for DAPQ-COF50 (48.8 Ω) compared to DAPQ-COF/CNT (59.3 Ω) was deduced from the electrochemical impedance spectroscopy (EIS) measurements of the electrodes (Figure 4d and Table S7, Supporting Information).

Figure 4d also shows the trend in the impedance characteristics of these composite materials as the proportion of CNTs utilized in the in situ polycondensation is increased. For all of the studied electrodes, the Nyquist plots consist of one depressed semicircle in the high-to-mid frequency range and a sloping line at mid-to-low frequencies. The semicircle reflects the charge-transfer resistance R_{ct} , which is related to reaction kinetics, and the sloping line reflects the diffusion process of Li^+ ions in the electrode (Warburg impedance). The equivalent circuit used to simulate the impedance spectra is shown in Figure S34, Supporting Information, and the fitting parameters are shown in Table S7, Supporting Information. DAPQ-COF50 has the smallest R_{ct} (48.8 Ω) in the DAPQ-COF and DAPQ-COFX electrodes, as well as the DAPQ-COF/CNT physical mixture. While the total proportion of CNTs in the electrode will affect bulk conductivities, these observed trends in impedance support the assertion of improved charge transfer in DAPQ-COF50 due to optimization of contact between the DAPQ-COF and conductive carbon network.

TEM and SEM images of DAPQ-COF/CNT are shown in Figure 4e,f, respectively. In contrast to DAPQ-COF50 with the tube-type core-shell structure (Figure 2i), DAPQ-COF/CNT prepared by ball milling features phase-separated larger COF particles and CNTs, with minor surface contacts observed between the physically mixed components. We suggest that this lack of a core-shell structure without the intimate surface contacts

between the COF and CNTs, as well as the larger COF particles and inefficient utilization of CNTs, accounts for the much lower utilization of the redox-active sites and poorer rate performance in DAPQ-COF/CNT.

2.4. Charge Storage Mechanism of DAPQ-COF

To identify the Li^+ storage sites during discharging process, ex situ FT-IR spectra of cycled DAPQ-COF50 electrodes were recorded. As depicted in Figure 5a, the bands at 1670 cm^{-1} , ascribed to the C=O groups in DAPQ structure, disappeared after discharging to 1.5 V. While a new signal at 1396 cm^{-1} , corresponding to the lithium enolate groups (C–O–Li), appeared when the electrode was fully discharged.^[7,9,46] The infrared spectra of the initial and fully recharged samples are identical, indicating the reversible and stable electrochemical reactions based on the C=O bonds during the charge–discharge process. Based on these results we proposed a mechanism as outlined in Figure 5b that involves redox reactions of both of the carbonyl groups in DAPQ, in agreement with previous reports.^[33,47]

To follow the nature of charge storage, the electrochemical reaction kinetics of DAPQ-COF50 were investigated by scanning the CV at various sweep rates (Figure 5c). The current response (i) of DAPQ-COF50 to the applied sweep rate (ν , 0.1–1.0 mV s^{-1}) was recorded. According to the power law, $i = a\nu^b$, b -values close to 0.5 indicate that the current is controlled by semi-infinite linear diffusion, by contrast, b -values close to 1 indicate that the current is surface-controlled. It is found that the b -values of four redox peaks R1, R2, O1, and O2

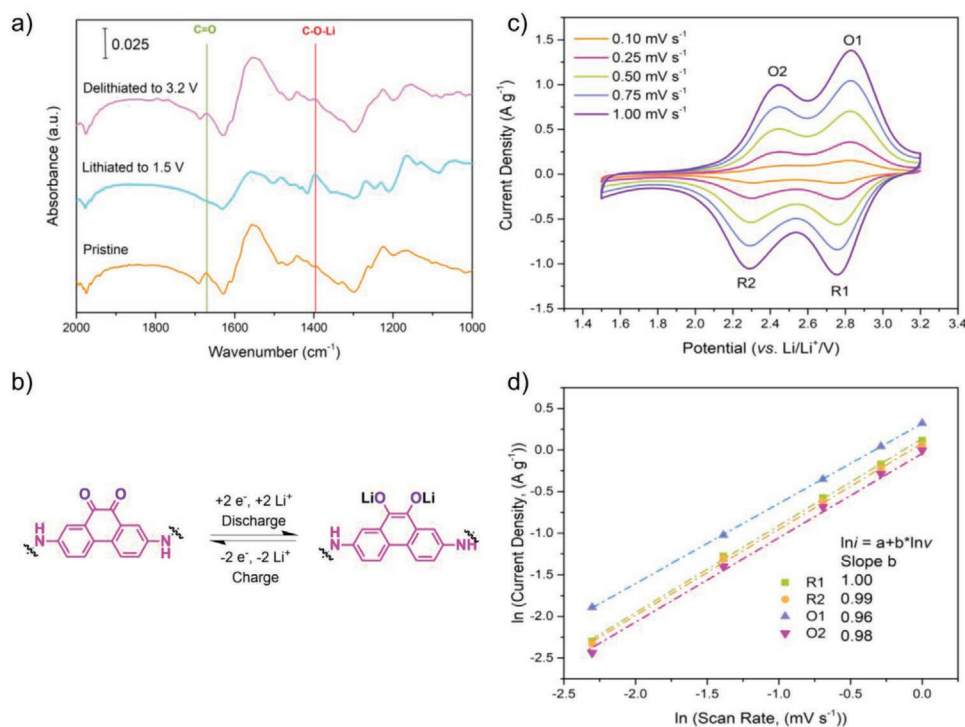


Figure 5. a) FT-IR Spectra of DAPQ-COF50 electrode materials at different states of lithiation/delithiation (pristine, lithiated to 1.5 V and delithiated to 3.2 V); b) Proposed reversible electrochemical redox mechanism of DAPQ-COF50 during the lithiation/delithiation process; c) CV of DAPQ-COF50 were collected at different scan rates; d) $\ln i$ versus $\ln \nu$ plots to determine the b values of different peaks.

(1.00, 0.99, 0.96, and 0.98) are all close to 1 (Figure 5d), indicating that the charge storage in DAPQ-COF50 is a fast surface-controlled process, which results from the high reactivity of carbonyl redox-active groups in DAPQ-COF50 not limited by ion diffusion within the studied sweep range. Further analysis of the voltammetric sweep rate dependence enables the surface-controlled contribution to the current response to be quantitatively distinguished.^[48] The current response at a fixed potential can be expressed as the combination of two separate mechanisms, namely surface-controlled contribution and diffusion-controlled insertion processes. In the equation of $i = k_1\nu + k_2\nu^{1/2}$, the exact surface-controlled contribution ($k_1\nu$) can be further quantified, where k_1 and k_2 constants can be simulated by plotting $i\nu^{-1/2}$ versus $\nu^{1/2}$, in which k_1 and k_2 are the slope and intercept, respectively, of the linear fitting plot (Figure S35, Supporting Information). At 0.1 mV s⁻¹, the surface contribution is determined to be 88%, which is further enhanced to 96% at 1.0 mV s⁻¹.

3. Conclusion

A β -ketoenamine-linked COF composite electrode was prepared by in situ polycondensation on CNTs. The synergy of the COF and the CNTs, where thin COF layers grow on the external surfaces of the CNTs, increased the charge transfer and electrochemical accessibility of active sites of the DAPQ-COF in the DAPQ-COFX composites. DAPQ-COF50 had the largest capacity of 162 mAh g⁻¹ at 500 mA g⁻¹, corresponding to 95% utilization of the redox-active sites. In addition, the optimized DAPQ-COF50 composite retained 76% of the capacity after 3000 cycles at 2000 mA g⁻¹ and exhibited excellent ultra-high rate performance, retaining 58% of its capacity at 50000 mA g⁻¹. This translates to a rate of 320 C, with charging times of 11 s, exceeding the rate capability of all previous reports for carbonyl-contained organic electrodes by an order of magnitude. DAPQ-COF50 exhibits a power density of 110 kW kg⁻¹, which is comparable to electrochemical capacitor materials. This remarkable performance is made possible by the synergistic effects of DAPQ-COF and CNTs and the synthetic route by which the core-shell nanotube structures are prepared. The open porous structures of the CNTs also facilitate the transport of ions to the reaction sites in the surrounding thin COF films. By optimizing the proportions of the COF and the CNTs in the reaction mixture, we can fabricate thinner layers of crystalline COF on the CNT surfaces, thus dramatically improving the electrochemical accessibility required to drive these redox reactions through ultrafast charge/discharge cycles with only a small drop in performance. An advantage of COFs as Li-ion battery materials over other porous organic materials, such as amorphous polymers, is their permanent, and atomistically tunable extended 3D structure and porosity. For Li-ion batteries, this is important because well-defined porosity can facilitate the diffusion of electrolytes to active sites embedded in the organic structures, to allow their utilization for charge storage. Extended π -systems in COFs have the added advantage of providing charge carrier transport pathways. These two properties combined make COFs a promising class of materials for energy storage applications. Furthermore, by growing COFs directly on

conductive carbon, we show that performance can be improved further by facilitating better utilization of the active sites and enhancing rate capabilities. This has the potential to create new applications in high-performance batteries, electrochemical capacitors, and fuel cells.

4. Experimental Section

Materials: 9,10-Phenanthrenequinone (PQ) and TFG were obtained from TCI. Acetic acid, palladium on carbon, catalyst-free multi-walled CNTs with outer diameter and length ranges of 7–15 nm and 0.5–10 μ m (CNTs, see Figure S1, Supporting Information, Raman spectra of CNTs), anhydrous *N*-methyl-2-pyrrolidone (NMP), polyvinylidene fluoride (PVDF), and isoquinoline were purchased from Sigma Aldrich. 1,4-dioxane, *n*-Butanol, and 1,2-dichlorobenzene (*o*-DCB) were obtained from Alfa-Aesar. Fuming nitric acid, sodium carbonate, dimethylacetamide (DMAC), and mesitylene were obtained from Acros Organics. Concentrated sulfuric acid, *N,N*-dimethylformamide (DMF), dimethyl sulfoxide (DMSO), acetone, and methanol were obtained from Fisher. All chemicals were used as received without further purification.

Synthesis of 2,7-Dinitro-9,10-phenanthrenequinone (DNPQ): DNPQ was synthesized according to a literature procedure.^[49] In a two-necked flask, PQ (2.0 g, 9.6 mmol) was added to a solution of fuming nitric acid (>90%, 28.0 mL) and concentrated sulfuric acid (95%, 2.8 mL). The reaction was heated under reflux for 2 h and then poured onto 500 mL of iced water. After cooling the reaction mixture to room temperature, the pH was adjusted to a neutral value by adding saturated sodium carbonate solution. The suspension was then removed by filtration to obtain the solid product, which was washed with deionized water. The product was finally recrystallized from acetic acid to afford DNPQ as a yellow precipitate in a yield of 38%: 1.1 g. ¹H NMR (400 MHz, DMSO-*d*₆, δ [ppm]): 8.75–8.70 (m, 4H), 8.62–8.56 (dd, $J_{\text{HH}} = 8.5, 2.5$ Hz, 2H). ¹³C {¹H} NMR (100 MHz, DMSO-*d*₆, δ [ppm]): 176.2, 148.8, 138.9, 134.0, 129.0, 128.1, 123.2. High-resolution mass spectrometry (HRMS): calcd. for [(C₁₄H₆N₂O₆)+Na]⁺: $m/z = 321.0118$; found: 321.0123.

Synthesis of DAPQ: DAPQ was synthesized according to a patent procedure.^[50] Palladium on carbon (10 wt% palladium, 100.0 mg) was added to a mixture of DNPQ (1.0 g, 3.35 mmol) in N₂ degassed methanol (100 mL). The reaction mixture was degassed with N₂ for 10 min and then purged with H₂ for 15 min. The reaction mixture was stirred at room temperature overnight under a positive pressure of H₂. Afterward, the suspension was filtered through Celite, which was then washed with methanol. The solvent was removed from the dark blue filtrate under reduced pressure to afford DAPQ as a black-colored precipitate in a yield of 88%: 0.7 g. ¹H NMR (400 MHz, DMSO-*d*₆): 7.71–7.50 (d, $J_{\text{HH}} = 8.6$ Hz, 2H), 7.16–7.02 (d, $J = 2.5$ Hz, 2H), 6.92–6.80 (dd, $J_{\text{HH}} = 8.5, 2.5$ Hz, 2H), 5.52 (s, 4H). ¹³C {¹H} NMR (100 MHz, DMSO-*d*₆, δ [ppm]): 181.1, 148.5, 130.6, 125.9, 124.7, 122.0, 113.3. HRMS: calcd. for [(C₁₄H₁₀N₂O₂)+Na]⁺: $m/z = 261.0634$; found: 261.0623.

Synthesis of DAPQ-COF: A 10 mL Pyrex tube (outer \times inner diameter = 1.3 \times 1.0 cm with a length 15 cm) was charged with TFG (10.5 mg, 0.05 mmol), DAPQ (17.9 mg, 0.075 mmol), mesitylene (0.9 mL), 1,4-dioxane (0.3 mL), and aqueous acetic acid (0.1 mL, 3 M). This mixture was homogenized by sonication for 10 min and the Pyrex glass tube was subjected to three freeze-pump-thaw cycles and evacuated to an internal pressure of 100 mTorr. The tube was sealed and then placed in an oven at 120 $^{\circ}$ C for 3 days. The black precipitate was collected by filtration and washed with DMF (3 \times 5 mL), DMSO (3 \times 5 mL), and acetone (3 \times 5 mL). The resulting solid was dried and then subjected to washing by Soxhlet extraction with methanol for 24 hours. The powder was collected and dried under reduced pressure at 85 $^{\circ}$ C to afford DAPQ-COF as a black powder in a yield of 91%: 22.6 mg.

Synthesis of DAPQ-COFX: A 10 mL Pyrex tube (outer \times inner diameter = 1.3 \times 1.0 cm with a length 15 cm) was charged with TFG (10.5 mg, 0.05 mmol), DAPQ (17.9 mg, 0.075 mmol), CNT (2.6, 10.0, and

23.4 mg, which corresponds to 10, 30, 50 wt% of CNT in the composites, respectively, assuming the DAPQ-COF yield from the composite reaction was also 91%), mesitylene (0.9 mL), 1,4-dioxane (0.3 mL), and aqueous acetic acid (0.1 mL, 3 M). This mixture was homogenized by sonication for 30 min and the Pyrex glass tube was subjected to three freeze-pump-thaw cycles and evacuated to an internal pressure of 100 mTorr. The tube was sealed and then placed in an oven at 120 °C for 3 days. The black precipitate was collected by filtration and washed with DMF (3 × 5 mL), DMSO (3 × 5 mL), and acetone (3 × 5 mL). The resulting solid was dried and then subjected to washing by Soxhlet extraction with methanol as the solvent for 24 h. The powder was collected and dried under reduced pressure at 85 °C to afford DAPQ-COFX as black powders. The yields calculated for DAPQ-COF10, DAPQ-COF30, and DAPQ-COF50 were 95, 92, and 89%, respectively.

Preparation of Electrodes and Electrochemical Characterization: The positive electrodes were prepared using the following procedure: The active material (DAPQ-COF or DAPQ-COFX) and carbon black (Super C65, IMERYS) were ground by pestle and mortar for 30 minutes. The solid was transferred into a small vial that was equipped with a stirrer bar. Poly(vinylidene fluoride) solution (5 wt% PVDF in NMP solution) was added to the vial. For the DAPQ-COF electrode, the mass ratio of DAPQ-COF, carbon black, and PVDF was 6:3:1. For the DAPQ-COFX electrodes, the mass ratio of DAPQ-COFX, carbon black, and PVDF were 7:2:1. Additional NMP was added to adjust the viscosity to form a slurry. After stirring the suspensions for 12 h, finely dispersed slurries were obtained and these were then coated onto aluminium foil substrates (thickness × width × height = 0.005 × 16 × 25 cm) using a doctor blade at a fixed thickness. The substrates were then dried at room temperature for 6 h followed by drying under vacuum pressure at 80 °C for 12 h to afford dry films. The films were then punched into discs with diameters of 10 mm. The discs were dried overnight under vacuum at 80 °C and transferred directly into a glovebox kept under an Ar atmosphere with H₂O and O₂ concentrations <0.1 ppm. The resulting electrode loadings were in the range of 0.3–0.6 mg cm⁻².

Coin cells (CR2025) were assembled inside an argon-filled glovebox. Lithium foil with a diameter of 12 mm and a thickness of 0.38 mm was used as the counter electrode, and glass microfiber (Whatman GF/F) was used as the separator. A mixture of 1,3-dioxolane and 1,2-dimethoxyethane (1:1 v/v) containing 1 M Li bis(trifluoromethanesulfonyl)imide (LiTFSI) was used as the electrolyte (Duoduo Chemicals). After preparation, the coin cells were taken out of the glovebox and tested.

CV (Biologic) plots were recorded over a potential range of 1.5–3.2 V (versus Li/Li⁺) at a scanning rate of 0.1 mV s⁻¹, starting from open circuit potential (2.7 V) to the cathodic scan (discharge) direction. The EIS (Biologic) measurements were carried out over a frequency range from 1 MHz to 100 mHz, with an amplified voltage of 10 mV. Galvanostatic discharge-charge cycling of the cells was measured within a potential window of 1.5–3.2 V (Maccor). All potentials are given versus Li/Li⁺. All electrochemical measurements were performed on the coin cells at 25 °C.

Supporting Information

Supporting Information is available from the Wiley Online Library or from the author.

Acknowledgements

The authors acknowledge the Engineering and Physical Sciences Research Council (EPSRC) (EP/N004884/1) and the Leverhulme Trust via the Leverhulme Research Centre for Functional Materials Design for funding. L.J.H. and A.R.N. acknowledge the EPSRC funding under grant EP/R020744/1. H.G. thanks the China Scholarship Council (CSC) for a scholarship. R.S.S. thanks the University of Strathclyde for financial support through The Strathclyde Chancellor's Fellowship Scheme. The

TEM analysis was performed in the Albert Crewe Centre for Electron Microscopy, a University of Liverpool Shared Research Facility.

Conflict of Interest

The authors declare no conflict of interest.

Data Availability Statement

The data that supports the findings of this study are available in the supplementary material of this article.

Keywords

covalent organic frameworks, Li-ion cells, positive electrode, ultra-high rate performance

Received: June 18, 2021

Revised: August 18, 2021

Published online:

- [1] J. Kim, J. H. Kim, K. Ariga, *Joule* **2017**, *1*, 739.
- [2] S. Muench, A. Wild, C. Friebe, B. Häupler, T. Janoschka, U. S. Schubert, *Chem. Rev.* **2016**, *116*, 9438.
- [3] Z. Song, H. Zhou, *Energy Environ. Sci.* **2013**, *6*, 2280.
- [4] M. Armand, J.-M. Tarascon, *Nature* **2008**, *451*, 652.
- [5] A. Jaffe, A. Saldivar Valdes, H. I. Karunadasa, *Chem. Mater.* **2015**, *27*, 3568.
- [6] H. Chen, M. Armand, M. Courty, M. Jiang, C. P. Grey, F. Dolhem, J. M. Tarascon, P. Poizot, *J. Am. Chem. Soc.* **2009**, *131*, 8984.
- [7] B. Tian, G.-H. Ning, W. Tang, C. Peng, D. Yu, Z. Chen, Y. Xiao, C. Su, K. P. Loh, *Mater. Horiz.* **2016**, *3*, 429.
- [8] H. Gao, B. Tian, H. Yang, A. R. Neale, M. A. Little, R. S. Sprick, L. J. Hardwick, A. I. Cooper, *ChemSusChem* **2020**, *13*, 5571.
- [9] Z. Ba, Z. Wang, M. Luo, H. B. Li, Y. Li, T. Huang, J. Dong, Q. Zhang, X. Zhao, *ACS Appl. Mater. Interfaces* **2020**, *12*, 807.
- [10] Z. Ouyang, D. Tranca, Y. Zhao, Z. Chen, X. Fu, J. Zhu, G. Zhai, C. Ke, E. Kymakis, X. Zhuang, *ACS Appl. Mater. Interfaces* **2021**, *13*, 9064.
- [11] N. W. Ockwig, A. P. Co, M. O. Keeffe, A. J. Matzger, O. M. Yaghi, *Science* **2005**, *310*, 1166.
- [12] Y. Zhang, J. Duan, D. Ma, P. Li, S. Li, H. Li, J. Zhou, X. Ma, X. Feng, B. Wang, *Angew. Chem., Int. Ed.* **2017**, *56*, 16313.
- [13] Z. Guo, Y. Zhang, Y. Dong, J. Li, S. Li, P. Shao, X. Feng, B. Wang, *J. Am. Chem. Soc.* **2019**, *141*, 1923.
- [14] D. Jiang, *Bull. Chem. Soc. Jpn.* **2021**, *94*, 1215.
- [15] F. Xu, S. Jin, H. Zhong, D. Wu, X. Yang, X. Chen, H. Wei, R. Fu, D. Jiang, *Sci. Rep.* **2015**, *5*, 8225.
- [16] K. Wang, Z. Jia, Y. Bai, X. Wang, S. E. Hodgkiss, L. Chen, S. Y. Chong, X. Wang, H. Yang, Y. Xu, F. Feng, J. W. Ward, A. I. Cooper, *J. Am. Chem. Soc.* **2020**, *142*, 11131.
- [17] G. Wang, N. Chandrasekhar, B. P. Biswal, D. Becker, S. Paasch, E. Brunner, M. Addicoat, M. Yu, R. Berger, X. Feng, *Adv. Mater.* **2019**, *31*, 1901478.
- [18] S. Xu, G. Wang, B. P. Biswal, M. Addicoat, S. Paasch, W. Sheng, X. Zhuang, E. Brunner, T. Heine, R. Berger, X. Feng, *Angew. Chem., Int. Ed.* **2019**, *58*, 849.
- [19] S. Jhulki, C. H. Feriante, R. Mysyk, A. M. Evans, A. Magasinski, A. S. Raman, K. Turcheniuk, S. Barlow, W. R. Dichtel, G. Yushin, S. R. Marder, *ACS Appl. Energy Mater.* **2021**, *4*, 350.

- [20] X. Feng, L. Liu, Y. Honsho, A. Saeki, S. Seki, S. Irle, Y. Dong, A. Nagai, D. Jiang, *Angew. Chem.* **2012**, *124*, 2672.
- [21] Z. Lei, Q. Yang, Y. Xu, S. Guo, W. Sun, H. Liu, L. P. Lv, Y. Zhang, Y. Wang, *Nat. Commun.* **2018**, *9*, 576.
- [22] Z. Wang, Y. Li, P. Liu, Q. Qi, F. Zhang, G. Lu, X. Zhao, X. Huang, *Nanoscale* **2019**, *11*, 5330.
- [23] S. Kandambeth, V. S. Kale, O. Shekhah, H. N. Alshareef, M. Eddaoudi, *Adv. Energy Mater.* **2021**, *31*, 2100177.
- [24] G. Zhao, H. Li, Z. Gao, L. Xu, Z. Mei, S. Cai, T. Liu, X. Yang, H. Guo, X. Sun, *Adv. Funct. Mater.* **2021**, *31*, 2101019.
- [25] Y. Huang, K. Li, J. Liu, X. Zhong, X. Duan, I. Shakir, Y. Xu, *J. Mater. Chem. A* **2017**, *5*, 2710.
- [26] D. Sui, L. Xu, H. Zhang, Z. Sun, B. Kan, Y. Ma, Y. Chen, *Carbon* **2020**, *157*, 656.
- [27] Z. Zhu, J. Chen, *J. Electrochem. Soc.* **2015**, *162*, A2393.
- [28] Z. Song, T. Xu, M. L. Gordin, Y. B. Jiang, I. T. Bae, Q. Xiao, H. Zhan, J. Liu, D. Wang, *Nano Lett.* **2012**, *12*, 2205.
- [29] S. Wang, Q. Wang, P. Shao, Y. Han, X. Gao, L. Ma, S. Yuan, X. Ma, J. Zhou, X. Feng, B. Wang, *J. Am. Chem. Soc.* **2017**, *139*, 4258.
- [30] Y. Tao, W. Ji, X. Ding, B. H. Han, *J. Mater. Chem. A* **2021**, *9*, 7336.
- [31] J. Li, X. Jing, Q. Li, S. Li, X. Gao, X. Feng, B. Wang, *Chem. Soc. Rev.* **2020**, *49*, 3565.
- [32] Y. Ishii, K. Tashiro, K. Hosoe, A. Al-Zubaidi, S. Kawasaki, *Phys. Chem. Chem. Phys.* **2016**, *18*, 10411.
- [33] Y. Liang, P. Zhang, J. Chen, *Chem. Sci.* **2013**, *4*, 1330.
- [34] S. Kandambeth, A. Mallick, B. Lukose, M. V. Mane, T. Heine, R. Banerjee, *J. Am. Chem. Soc.* **2012**, *134*, 19524.
- [35] C. R. Deblase, K. E. Silberstein, T.-T. Truong, H. D. Abruña, W. R. Dichtel, *J. Am. Chem. Soc.* **2013**, *135*, 16821.
- [36] W. Xu, A. Read, P. K. Koech, D. Hu, C. Wang, J. Xiao, A. B. Padmaperuma, G. L. Graff, J. Liu, J. G. Zhang, *J. Mater. Chem.* **2012**, *22*, 4032.
- [37] E. Vitaku, C. N. Gannett, K. L. Carpenter, L. Shen, H. D. Abruña, W. R. Dichtel, *J. Am. Chem. Soc.* **2020**, *142*, 16.
- [38] J. Lv, Y. X. Tan, J. Xie, R. Yang, M. Yu, S. Sun, M. De Li, D. Yuan, Y. Wang, *Angew. Chem., Int. Ed.* **2018**, *57*, 12716.
- [39] Z. Luo, L. Liu, J. Ning, K. Lei, Y. Lu, F. Li, J. Chen, *Angew. Chem., Int. Ed.* **2018**, *57*, 9443.
- [40] S. Lee, J. E. Kwon, J. Hong, S. Y. Park, K. Kang, *J. Mater. Chem. A* **2019**, *7*, 11438.
- [41] W. Ma, L. Luo, P. Dong, P. Zheng, X. Huang, C. Zhang, J. Jiang, Y. Cao, *Adv. Funct. Mater.* **2021**, 2105027, <https://doi.org/10.1002/adfm.202105027>.
- [42] D. H. Yang, Z. Q. Yao, D. Wu, Y. H. Zhang, Z. Zhou, X. H. Bu, *J. Mater. Chem. A* **2016**, *4*, 18621.
- [43] C. J. Yao, Z. Wu, J. Xie, F. Yu, W. Guo, Z. J. Xu, D. S. Li, S. Zhang, Q. Zhang, *ChemSusChem* **2020**, *13*, 2457.
- [44] X. Li, Y. Li, K. Sarang, J. Lutkenhaus, R. Verduzco, *Adv. Funct. Mater.* **2021**, *31*, 2009263.
- [45] F. Béguin, V. Presser, A. Balducci, E. Frackowiak, *Adv. Mater.* **2014**, *26*, 2219.
- [46] Z. Song, Y. Qian, M. L. Gordin, D. Tang, T. Xu, M. Otani, H. Zhan, H. Zhou, D. Wang, *Angew. Chem., Int. Ed.* **2015**, *54*, 13947.
- [47] H. Wang, C.-J. Yao, H.-J. Nie, K.-Z. Wang, Y.-W. Zhong, P. Chen, S. Mei, Q. Zhang, *J. Mater. Chem. A* **2020**, *8*, 11906.
- [48] J. Wang, J. Polleux, J. Lim, B. Dunn, *J. Phys. Chem. C* **2007**, *111*, 14925.
- [49] V. Bravo, S. Gil, A. M. Costero, M. N. Kneeteman, U. Llaosa, P. M. E. Mancini, L. E. Ochando, M. Parra, *Tetrahedron* **2012**, *68*, 4882.
- [50] T. Health, W. Timothy, W. Zhan, *WO2019084452A1*, **2018**.